Journal of Sol-Gel Science and Technology
https://doi.org/10.1007/s10971-024-06342-8

ORIGINAL PAPER

Electrochromic windows based on luminescent acrylate/ionosilicas

Daniela Pinheiro[1,6] · **Rui F. P. Pereira**[2] · **Alexandra Gonçalves**[3] · **Sandra F. H. Correia**[4] · **M. Manuela Silva**[2] · **Elvira Fortunato**[3] · **Maria Cristina Gonçalves**[1] · **Rute A. S. Ferreira**[5] · **Verónica de Zea Bermudez**[1]

Received: 29 September 2023 / Accepted: 8 February 2024

Abstract

Poly(methyl methacrylate) (PMMA)-based composite films doped with lanthanide-doped sol–gel derived imidazolium-based ionosilicas (IS-Ln) were recently proposed as active layers of luminescent down shifting (LDS) layers, but subsequent work demonstrated also their potential as electrolytes for electrochromic devices (ECDs) with foreseen application in smart windows of energy-efficient buildings. Nevertheless, some challenges remained to be addressed in the latter devices, the most critical one being the poor solubility of PMMA in the ionic liquid used in the formulation of these materials. To avoid this drawback, in the present work we propose novel lanthanide-containing acrylate/ionosilicas (AC/IS-Ln, Ln = Tb^{3+}, Eu^{3+}). The transparent, homogeneous, and luminescent hybrid materials synthesized are characterized by Fourier transform infrared spectroscopy, X-ray diffraction, thermogravimetric analysis, atomic force microscopy, contact angle measurements, ionic conductivity, and photoluminescence spectroscopy. Optimized samples are successfully employed as electrolytes in luminescent ECD prototypes. The ECD device doped with AC/IS-Eu shows good cycling stability with reproducible bleaching/coloring over 50 chronoamperometry cycles, high coloration efficiency (CE) values CE_{in}/CE_{out} in the visible ($-89/+98\ cm^2\ C^{-1}$), and near-infrared ($-126/138\ cm^2\ C^{-1}$) spectral regions, and outstanding memory effect.

Graphical Abstract

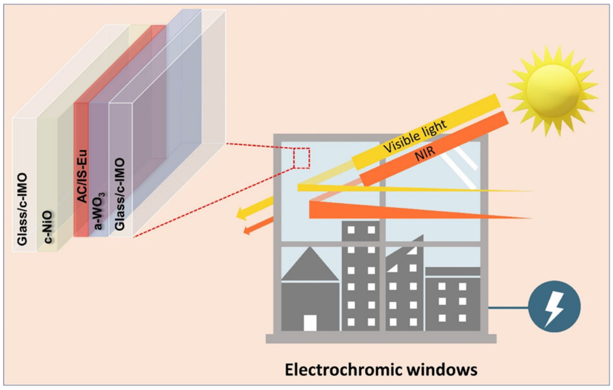

✉ Daniela Pinheiro
danielap@utad.pt

✉ Verónica de Zea Bermudez
vbermude@utad.pt

[1] Chemistry Department and CQ-VR, University of Trás-os-Montes e Alto Douro, 5000-801 Vila Real, Portugal

[2] Chemistry Department and Centre of Chemistry, University of Minho, 4710-057 Braga, Portugal

[3] CENIMAT/I3N, Departamento de Ciência dos Materiais, Faculdade de Ciências e Tecnologia, 2829-516 Lisboa, Portugal

[4] Instituto de Telecomunicações, University of Aveiro, 3810-193 Aveiro, Portugal

[5] Physics Department and CICECO—Aveiro Institute of Materials, University of Aveiro, 3810-193 Aveiro, Portugal

[6] Present address: CPIRN-IPG—Center of Potential and Innovation of Natural Resources, Polytechnic of Guarda, 6300-559 Guarda, Portugal

Keywords Sol–gel · Luminescent acrylate/ionosilicas · Visible and NIR emitting electrolytes · Electrochromic smart windows

Highlights

- Novel lanthanide-containing acrylate/ionosilicas (AC/IS-Ln) were synthesized by sol–gel chemistry.
- An optimized AC/IS-Eu hybrid was successfully applied as an electrolyte in an electrochromic device prototype.
- The prototype device demonstrated excellent electro-optical performance (good cycling stability, high coloration efficiency, and outstanding memory effect).

1 Introduction

The building sector is one of the most energy-consuming economic sectors. In the European Union (EU), buildings are responsible for *ca*. 40% of the primary energy consumption and for about 36% of global greenhouse gas (GHG) emissions [1]. Half of the energy consumption in residential and commercial buildings is known to be associated with heating, cooling, and lighting, but the use of energy consumption in each building depends on its orientation, geographical location, climate region, the season of the year, and the time of the day. To transition to decarbonized energy-efficient buildings, the European Commission (EC) made energy performance a top priority concern. It developed through the years a series of energy policies that led to the implementation of three directives: the 2020 Climate and Energy Package [1], related to the Energy Efficiency Directive (1) [2], the 2030 Climate and Energy Framework (2) [3], and the 2050 Long-Term Strategy (3) [4], which targets climate neutrality by 2050 and net-zero GHG emissions. More recently, the EC proposed the zero-emission building (ZEB) construction concept [5], thus aligning the energy performance requirement to the longer-term climate neutrality goal. All these actions are aligned with the Paris Agreement [6], the European Green Deal [7], and the United Nations Sustainable Development Goals for 2030. These are “the blueprint to achieve a better and more sustainable future for all” [3]. The Sustainable Development Goals 7—Affordable and Clean Energy, 11—Sustainable Cities and Communities, and 13—Climate Action, aim at developing energy-efficient buildings for a thriving, sustainable, climate-neutral, resilient, safe, and healthy society.

To fulfill the energy and sustainability requirements, the building sector needs to fabricate and install energy-efficient envelopes (external walls, floors, roofs, ceilings, windows, and doors). Among the components of the building envelope, windows contribute a significant 10% of the total energy consumed. It has long been recognized that the substitution of conventional (static) windows for smart (dynamic) windows will potentially impact energy savings.

Thanks to a combination of function and aesthetics, electrochromic windows (ECWs) are among the most attractive window technological solutions for extensive glass façades [8, 9]. Apart from mitigating energy needs of the ZEBs of future smart cities, ECWs enable the occupant to control light and heat transmission, increasing indoor thermal and visual comfort, while improving outdoor view [4–8], making blinds and curtains useless. These switchable windows grant architects with considerable freedom in terms of shape and color, resulting in buildings with enhanced aesthetics.

One of the most widely adopted configurations for electrochromic devices (ECDs) is the layered battery-like one, in which 5 functional layers are assembled in a sandwich-like structure [10]. Upon application of an external low electric voltage (usually 1.0–3.0 V), such devices can modulate the transmission of sunlight and solar heat gain. In practice, the optical transparency is switched reversibly between colored/bleached states, and the heat is admitted/blocked, respectively, at the user’s choice. Good examples of commercially successful ECWs are the Gentex EC portholes, which allow passengers of the Boeing 787 Dreamliner to adjust the glare and improve their comfort level inside the aircraft, and the Ambilight Inc. ECD sunroofs for electrical vehicles.

Over the last few years, various integrated device solutions have been proposed for solar energy management. An attractive concept is the combination of ECWs with solar cells [11] and building integrated photovoltaics (BIPVs) [12]. PV-powered ECWs are an efficient way to improve the efficiency of the windows and reduce the consumption of energy, since the requirement of an external electrical supply is no longer required [13, 14]. Kou et al. [13] were the first to report an integrated system combining nickel-cobalt bimetal oxide ECW and a $Cu_2ZnSn(S,Se)_4$ (CZTSSe) thin-film solar cell. The self-powered EC energy storage smart window demonstrated excellent optical modulation, and fast coloration speed. Among different PV technologies, dye-sensitized solar cells (DSSCs) and perovskite solar cells (PSCs) have received great attention. DSSCs, first introduced by Grätzel and O’Regan [15], provide a cost-effective and efficient alternative to the first generation of crystalline Si-based solar panels [16]. Recently, notable advances have been made in DSSCs in terms of design and power conversion efficiency [17–20]. Gianola et al. [19]

proposed a new configuration, called homo-tandem-bifacial (HTB)-DSSC, that can surpass the maximum efficiency ever obtained for traditional DSSCs, presenting photoconversion efficiency (PCE) values of 20–22% and a 37% increase in the PV performance. In recent years, due to the excellent PCE values (improvement from 4 to 26%) and enormous potential as a competitive alternative to conventional solar cell technologies, interest rapidly shifted from DSSCs to PSCs [21, 22]. Three major categories of PSCs were explored aiming applications in BIPVs: semi-transparent, colorful, and smart PV windows [21]. Zhang et al. [23] proposed a PV modular ECW composed of three areas (PV, ECD, and transparent layer) that can adjust the position of each other. Compared to normal windows, this system was able to save up to 15.79% of energy.

Recently, based on the fact that the efficiency of PV cells is potentially improved through coupling with luminescent down-shifting (LDS) layers and luminescent solar concentrators (LSCs) [24], the sol–gel method was employed to synthesize new luminescent films aiming at the fabrication of LSC-LDS/PV/ECD systems for energy harvesting/conversion/management. The materials were first tested in LSCs [25]. The same type of film was then successfully used first in a combined LSC-LDS/PV configuration working simultaneously as LDS and LSC layers, and then in LDS solar spectral conversion [26]. In both cases, the active films were composed of a poly(methyl methacrylate) (PMMA) matrix to which Ln-doped ionosilicas (ISs) were added. The materials were noted as IS-Ln-X, where Ln = Nd^{3+}, Eu^{3+}, Tb^{3+}, and Yb^{3+}, and X = IS-Ln/PMMA w/w. The IS comprised a silica matrix covalently bonded to 1-butyl-3-methylimidazolium ($[Bmim]^+$) cations, the counter ions of which were the $[Ln(tta)_4]^-$ complex anions (where tta^- is 2-thenoyltrifluoroacetonate). The selection of PMMA was logical. It is one of the most widely used host materials for the development of LSCs. This low-cost and non-toxic thermoplastic has high optical transparency under solar irradiation, high thermal stability in a wide range of temperatures (−70 to 100 °C), high scratch resistance, notorious high resistance to UV radiation exposure and several chemical treatments, exceptional performance in all weather conditions, higher impact resistance than glass, and easy handling and processing. Another useful attribute of PMMA is the fact that it is compatible with liquid electrolytes, such as ionic liquids (ILs) [27].

More recently, the above formulation was adapted to provide the proof-of-concept that demonstrated that this active layer can act as the electrolyte in an ECD including the complementary electrochromic electrodes amorphous tungsten oxide (a-WO_3) and crystalline nickel oxide (c-NiO), and the amorphous indium zinc oxide (a-IZO) external conducting layers, which are transparent over the visible-to-NIR region [28]. The electrolyte comprised, apart from PMMA, IS-Nd, and IS-Eu, the 1-butyl-3-methylimidazolium hexafluorophosphate ($[BMIm][PF_6]$) ionic liquid (IL). The latter compound was added to increase the ionic conductivity, act as plasticizer, and dissolve PMMA. At 555/1650 nm, the red/NIR-emitting device exhibited fast switching speed (50 s) and transmittance (*T*) values of 79/77% in the as-prepared state. After 200 cycles at ±2.5 V, $T_{\text{bleached}}/T_{\text{colored}}$ values of 44/28 and 27/9%, and coloration efficiency (CE) values of CE_{in}/CE_{out} values $-302/+181$ and $-734/+440\ cm^2\ C^{-1}$, resulted at 555 and 1650 nm, respectively. We found that the presence of the $[Nd(tta)_4]^-$ and $[Eu(tta)_4]^-$ anions had a dual role, imparting the NIR and red emitting features, respectively, and increasing solar radiation durability. In fact, due to the absorption of the tta^- ligand in the UV region of the solar spectrum, PMMA yellowing is avoided.

In the present work, to further improve the performance of the above ECD concept, we decided to remove PMMA from the formulation and use exclusively sol–gel derived materials. To promote the homogeneity, 3-(acryloyloxy) propyltrimethoxysilane), an alkoxysilane analog of PMMA, was polycondensed with the silica precursor, using *N,N'*-dimethylformamide (DMF) and dimethylsulfoxide (DMSO) as solvents. The resulting transparent, luminescent Tb^{3+}, Eu^{3+}-doped acrylate/ionosilica electrolytes were noted as AC/IS-Ln. Their structure, morphology, ionic conductivity, thermal behavior, and optical properties were characterized. The electrolyte with the highest ionic conductivity (AC/IS-Eu, $2.39 \times 10^{-6}\ S\ cm^{-1}$ at 19 °C) was used to assemble an ECD prototype with a configuration identical to that used previously, except for the a-IZO layers which were replaced by crystalline indium molybdenum oxide (c-IMO), which is also transparent in the visible-to-NIR spectral region [28, 29]. To the best of our knowledge, this is the first report of an ECD containing electrolytes composed of AC/IS doped with lanthanides. The results show that the ECD exhibits excellent cycling stability and open-circuit memory with only 7% transmittance loss over 60 days.

2 Experimental

2.1 Materials

Thenoyltrifluoroacetone (Htta, 99%, Sigma-Aldrich), terbium(III) chloride hexahydrate ($TbCl_3·6H_2O$, 99.9%, Alfa Aesar), europium(III) chloride hexahydrate ($EuCl_3·6H_2O$, 99.99%, TCI), *N*-butylimidazole (BIm, 98%, Sigma-Aldrich), (3-chloropropyl)trimethoxysilane (CPTMS, 97%, Sigma-Aldrich), 3-(acryloyloxy)propyltrimethoxysilane (ACPTMS, 94%, Thermo Scientific), anhydrous ethyl acetate (EtOAc, 98.8%, Sigma-Aldrich), ethanol (EtOH, 99.8%, Fluka), *N,N'*-dimethylformamide (DMF, 99.5%, HPLC grade, Fluka), dimethylsulfoxide (DMSO, Fluka), sodium hydroxide (NaOH, Merck), and diiodomethane (99%, stab. CH_2I_2, Thermo Scientific) were used as received. Ultra-pure water at pH = 5.4 was used in all experiments.

2.2 Synthesis

2.2.1 Synthesis of sodium tetra(2-thenoyltrifluoroacetonate) terbate (III)/europate(III) ($Na[Ln(tta)_4]$ with Ln = Tb^{3+}, Eu^{3+})

The lanthanide complex ($Na[Ln(tta)_4]$ (Ln = Tb^{3+}, Eu^{3+}) was prepared using the conventional method described elsewhere [25].

A mass of 0.889 g of Htta was dissolved in 5 mL of EtOH and then deprotonated with 0.16 g NaOH at 50–60 °C for 2 h. To this solution, 1 equivalent of $LnCl_3{\cdot}6H_2O$, dissolved in 5 mL of EtOH, was added dropwise (molar ratio Htta:NaOH:$LnCl_3{\cdot}6H_2O$ = 4:4:1). After keeping the mixtures at 50–60 °C for 1 h, EtOH was evaporated under reduced pressure in a rotary evaporator and the as-produced salts were dried for 3 days at 60 °C (Fig. S1).

2.2.2 Synthesis of 1-butyl-3-[3-(trimethoxysilyl)propyl] imidazolium chloride ([B(TMSP)Im]Cl)

This compound was synthesized following a previously reported procedure [25].

BIm was mixed with CPTMS (molar ratio BIm:CPTMS = 1:1) and stirred at 70 °C for 5 days under nitrogen atmosphere (Fig. S2). The resulting pale-yellow viscous product was washed thrice with anhydrous EtOAc (10 mL). It was then dried under vacuum to remove excess EtOAc and finally stored under vacuum conditions.

2.2.3 Synthesis of 1-butyl-3-[3-(trimethoxysilyl)propyl] imidazolium tetra(2- thenoyltrifluoroacetonate) terbate(III)/europate(III) ($[B(TMSP)Im][Ln(tta)_4]$ with Ln = Tb^{3+}, Eu^{3+}

The lanthanide complex ($Na[Ln(tta)_4]$ (Ln = Tb^{3+}, Eu^{3+}) dissolved in 10 ml of DMF/DMSO (1:1 V/V) was reacted with [B(TMSP)Im]Cl (molar ratio $Na[Ln(tta)_4]$:[B(TMSP)Im]Cl = 1:1) (Fig. S3). The resulting mixture was stirred for 24 h at room temperature under nitrogen atmosphere. Sodium chloride (NaCl) was removed from the solution by precipitation and centrifugation (3 × 30 min, 4000 rpm).

2.2.4 Synthesis of the lanthanide-doped acrylate/ionosilicas (AC/IS-Ln with Ln = Tb^{3+}, Eu^{3+})

A mass of 5 g of ACPTMS was dissolved in 10 mL of DMF/DMSO (volume ratio DMF:DMSO = 1:1). Then, 0.5 g of [B(TMSP)Im]Cl and 0.5 g DMF/DMSO solution of $[B(TMSP)Im][Ln(tta)_4]$) (Ln = Tb^{3+}, Eu^{3+}) were added to the mixture. The resulting mixture was stirred for 5 min and water and EtOH were added (molar ratio $[B(TMSP)Im][Ln(tta)_4]$:EtOH:H_2O = 1:4:1.5) to initiate the sol–gel process. This mixture was stirred in a sealed flask for ~30 min, cast into a Teflon mold, covered with parafilm and left in a fume cupboard for 24 h (Fig. S4). The Teflon mold was subsequently transferred to an oven at 60 °C and the resulting AC/IS-Ln sample, produced as a glassy monolith with a yellowish hue, was aged for a period of 4 weeks. For comparison purposes, a non-doped sample, using only 5 g of ACPTMS and 0.5 g of [B(TMSP)Im]Cl was also synthetized (AC/IS). Elemental analysis: AC/IS-Tb ($C_{54}H_{72}F_{12}N_2O_{16}S_4Si_2Tb$) Calculated: C, 41.14; H, 4.60; N, 1.78. Found: C, 41.51; H, 5.16; N, 1.43; AC/IS-Eu ($C_{54}H_{72}F_{12}N_2O_{16}S_4Si_2Eu$) Calculated: C, 41.32; H, 4.62; N, 1.78. Found: C, 41.61; H, 5.88; N, 1.76; AC/IS ($C_{22}H_{48}ClN_2O_8Si_2$) Calculated: C, 47.16; H, 8.64; N, 5.00. Found: C, 42.97; H, 6.46; N, 1.05.

2.3 Characterization

Elemental analysis (CHN) was performed with a TruSpec 630-200-200 CNHS Analyzer with an accuracy of 1% for each element.

Attenuated total reflection Fourier transform infrared (ATR/FT-IR) spectra were acquired at room temperature with a Thermo Scientific Nicolet S50 FT-IR spectrometer, equipped with an ATR accessory with a diamond crystal. The instrument was controlled by the Omnic software package (version 9.2.28) from Thermo Fisher Scientific, Inc. The spectra were collected in the 4000–400 cm^{-1} range by averaging 180 scans at a resolution of 4 cm^{-1}.

The X-ray diffraction (XRD) patterns were recorded in the 2θ range spanning from 3° to 60° by using a PANalytical Empyrean diffractometer system with CuKα radiation ($\lambda = 1.54$ Å) at room temperature. The spacing between planes in the atomic lattice (d) was calculated using Bragg's law equation (Eq. (1)):

$$nd = 2\,d\,\sin\theta \quad (1)$$

where n is an integer, λ is the incident X-ray wavelength, and θ is the diffraction angle in degrees.

Thermogravimetric analysis (TGA) measurements were performed using Netzsch equipment (model STA 449 F3 Jupiter) and Proteus software version 7.1. A small piece of the sample (mass of ~10 mg) was placed into an alumina crucible. The thermogram was recorded during heating from room temperature to 700 °C at 10 °C min^{-1}. The purge gas used in all experiments was high-purity nitrogen (N_2) supplied at a constant 20 mL min^{-1} flow rate.

The wettability of the samples was assessed through static contact angle measurements using the sessile drop method. Contact angles were measured in a temperature-controlled chamber at 25 ± 1 °C using a Krüss DSA25S drop-shape analyzer controlled by the software ADVANCE. The volume of the liquid droplets was kept constant at 5 μL. Contact angles were measured using digital images acquired by a video camera using the Young-Laplace fitting. The contact angle values were measured at five different spots. At each spot, ten measurements were performed. The reported results correspond to the average value of all the measurements. The error analysis of the data was implemented by the arithmetic mean of the root mean square error.

The surface free energy (SFE) and its dispersive and polar components were determined by the contact angle technique using water and diiodomethane. To calculate the SFE of the solid surfaces of AC/IS, AC/IS-Tb, and AC/IS-Eu contact angle values, we used the Owens, Wendt, Rabel, and Kaelble (OWRK) method [30, 31]. The OWRK method implies the use of the following equation (Eq. (2)):

$$\gamma_{\mathrm{LV}}(1+\cos\theta)=2\left(\sqrt{\gamma_{\mathrm{LV}}^{\mathrm{d}}\gamma_{\mathrm{SV}}^{\mathrm{d}}}+\sqrt{\gamma_{\mathrm{LV}}^{\mathrm{p}}\gamma_{\mathrm{SV}}^{\mathrm{p}}}\right) \tag{2}$$

where γ_{LV}, the surface tension between the liquid and vapor (air), is the sum of a dispersive component ($\gamma_{\mathrm{LV}}^{\mathrm{d}}$, e.g. London dispersion forces) and polar component ($\gamma_{\mathrm{LV}}^{\mathrm{p}}$, e.g. hydrogen bonding). Likewise, $\gamma_{\mathrm{SV}}^{\mathrm{d}}$ and $\gamma_{\mathrm{SV}}^{\mathrm{p}}$ are the dispersive and polar components of γ_{SV} (or SFE), respectively. Equation (2) is used to calculate the unknown values $\gamma_{\mathrm{SV}}^{\mathrm{d}}$, $\gamma_{\mathrm{SV}}^{\mathrm{p}}$, and γ_{SV} (i.e., SFE). The method relies on contact angle measurements with at least two test liquids with known $\gamma_{\mathrm{LV}}^{\mathrm{d}}$ and $\gamma_{\mathrm{LV}}^{\mathrm{p}}$ values. One of these liquids must be predominantly polar and the second liquid should be dispersive (typically water and diiodomethane, respectively). It should be noted that the OWRK model implies the use of a high purity liquid, a smooth and chemically homogenous solid, and the absence of chemical reactions between the liquid and the solid. The OWRK model is a powerful model that has found widespread acceptance both in research and industry contexts. The relationship between SFE, γ_{LV}, and contact angle may be visualized using the so-called wetting envelope plots. These are based on the OWRK equation, but rewritten in terms of polar coordinates. The wetting envelopes of the two electrolytes studied were built using the Excel spreadsheet provided by Nanoscience [32].

The atomic force microscopy (AFM) measurements were performed in a Nano-Observer AFM microscope (CSInstruments AFM Microscopes-France) in tapping mode. A super sharp Si HQ:NSC19/FORTA probe with a frequency resonance of 60 kHz and a spring constant of 0.3 N m^{-1} was employed. Flattening and elimination of line noise tools and a lowpass filter provided by the Gwyddion 2.61 software were performed to improve the quality of the images.

The ionic conductivity of the samples was calculated by complex impedance measurements. A sample disk was placed between two 10 mm diameter ion blocking gold electrodes (Goodfellow, >99.9%). The electrode/electrolyte/electrode assembly was secured in a suitable constant volume support installed in a Buchi TO51 tube oven and the sample temperature was evaluated by a type K thermocouple placed close to the ormolyte disk. Samples were characterized over a temperature range of between 17 and 99 °C. Bulk conductivities of the samples were obtained during heating cycles using the complex plane impedance technique (Autolab PGSTAT-12 (Eco Chemie)) over a frequency range of 65 kHz to 0.5 Hz.

Scanning electron microscopy (SEM) analyses were performed at the Iberian Nanotechnology Laboratory using a FEI Quanta 650 FEG microscope under high vacuum. Secondary electrons were detected by an Everhardt Thornley SED (secondary electron detector). The images were acquired at 15 kV and spot size 3 nm. The samples were sputtered with gold, using the Leica EM ACE200 and using the following setup: sputtering current = 30 mA and duration = 60 s.

The photoluminescence spectra were recorded at room temperature with a modular double-grating excitation spectrofluorimeter with a TRIAX 320 emission monochromator (Fluorolog-3, Horiba Scientific) coupled to an R928 Hamamatsu photomultiplier. The excitation source was a 450 W Xe arc lamp. The emission spectra were corrected for detection and optical spectral response of the spectrofluorimeter and the excitation spectra were corrected for the spectral distribution of the lamp intensity using a photodiode reference detector. Emission decay curves were recorded at room temperature on a Fluorolog TCSPC spectrofluorometer (Horiba Scientific) coupled to a TBX-04 photomultiplier tube module (950 V) and a 200×10^{-9} s time-to-amplitude converter with a delay of 70×10^{-9} s. The excitation source was a Horiba/Jobin-Yvon pulsed diode (SpectraLED-355, peak at 355 nm, 1×10^{-7} s pulse duration). The absolute emission quantum yield (Φ) values were measured at room temperature using a C9920-02 Hamamatsu system. The method is accurate within 10%.

2.4 Assembly of the ECD

The ECD prototype was designed with the five-layer configuration glass/c-IMO/a-$\mathrm{WO_3}$/AC/IS-Eu/c-NiO/c-IMO/glass (Fig. 1). The active EC layers of the device (a-$\mathrm{WO_3}$ and c-NiO) were deposited on the glass by sputtering and e-beam evaporation, respectively. The c-IMO thin films were deposited by radio frequency (r.f.) magnetron sputtering at room temperature, using a ceramic target (99.99%) (Super

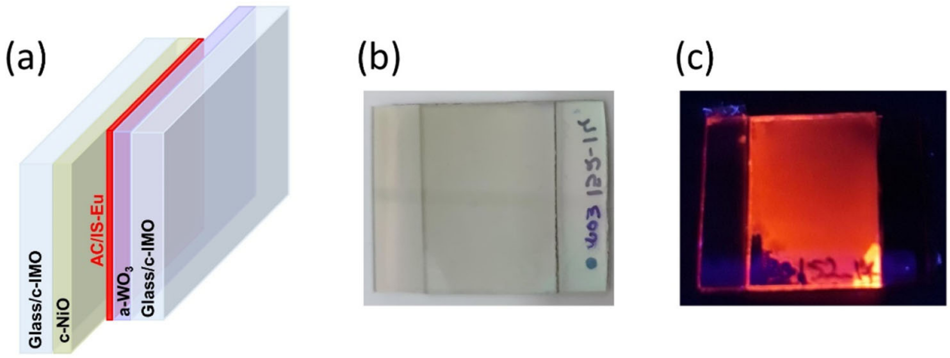

Fig. 1 Glass/c-IMO/a-WO_3/AC/IS-Eu/c-NiO/c-IMO/glass ECD configuration. Schematic representation (**a**). Assembled ECD as-prepared: under daylight (**b**) and UV light (365 nm) (**c**)

Conductor Materials, Inc., USA, In_2O_3 (98 wt%):Mo (2 wt%)) and soda-lime glass substrates (100 mm^3 × 100 mm^3 × 1 mm^3) [29]. The a-WO_3 was produced in a Pfeiffer Vacuum Classic 500 system using 3 diameter ceramic target from Plasmaterials, an argon and oxygen atmosphere (oxygen partial pressure of 0.2 Pa) and a deposition pressure of 1.0 Pa, under a r.f. power of 200 W, achieving a thickness of 300 nm. A polycrystalline c-NiO thin film was deposited by e-beam evaporation in a homemade system, from NiO commercial pellets with random dimensions of 3–6 mm (99.99%, Super Conductive Materials), with an initial chamber pressure of 7×10^{-4} Pa and growth rate of 6 nm min^{-1}, reaching a thickness of 300 nm.

An ECD prototype with 1.8×2.5 cm^2 active area was assembled under atmospheric conditions. A small volume of AC/IS-Eu sol was directly cast onto the surface of a-WO_3/c-IMO sputtered coated glass plate. After solvent evaporation, a c-NiO/c-IMO-sputtered coated glass plate was placed on the top of it so that the two coatings faced each other, leaving free space on one side of each glass plate to ensure the electrical contacts. The assembled plates of the device, denoted as ECD@AC/IS-Eu, were then pressed together and left standing prior to the electro-optical analyses. A replica of this ECD prototype was assembled and tested for reproducibility purposes.

2.5 Characterization of the ECD

The optical transmittance (T) of ECD@AC/IS-Eu was measured in the 400–1650 nm range using a DH Mini, UV-Vis-NIR Lightsource Ocean Optics and a halogen lamp. Cyclic voltammetry (CV) and chronoamperometry (CA) tests were carried out using a Gamry ZRA 11107 potentiostat/galvanostat.

In the setup used for measurements, the a-WO_3/c-IMO substrate played the role of working electrode, the AC/IS-Eu acted as a reservoir of ions, and the c-NiO/c-IMO substrate acted as counter and reference electrodes. The cathodic and anodic charge densities were determined through integration of the CA curves during the coloring and bleaching processes, respectively.

The performance of the ECD@AC/IS-Eu was evaluated following several technical parameters: switching speed (time required for the coloring/bleaching process), switching efficiency (optical contrast measured by the transmittance change $\Delta T = T_{\text{bleached}} - T_{\text{colored}}$, in %, at a given wavelength), optical density (optical modulation measured by $\Delta \text{OD} = -\log\ (T_{\text{colored}}/T_{\text{bleached}})$), coloration efficiency ($\text{CE} = \Delta \text{OD}/\Delta Q$, where Q is the inserted/desinserted charge density), cycling stability, and optical memory test.

The Commission Internationale d'Éclairage (CIE) 1976 L*a*b* color coordinates (where L* is the lightness (0 = black, 100 = diffuse white), a* is a red-green balance (+a* = red and −a* = green hues), and b* is a yellow-blue balance (+b* = yellow and −b* = blue hues) were obtained in the bleached and colored states with a Chroma Meter CR-300 Minolta (Osaka, Japan). The L*, a*, and b* parameters were calculated from the average values obtained from three independent measurements in different places of the window. The standard deviation was below 2%.

3 Results and discussion

3.1 Physical-chemical characterization

The AC/IS-Ln monoliths were prepared as transparent and luminescent films (Fig. 2).

The ATR/FTIR spectra of ACPTMS, [B(TMSP)Im]Cl, AC/IS, AC/IS-Tb, and AC/IS-Eu in the 4000–400 cm^{-1} region are depicted in Fig. 3a.

These spectral data confirmed the successful synthesis and incorporation of [B(TMSP)Im]Cl and [B(TMSP)Im][Ln(tta)$_4$] (Ln = Tb^{3+}, Eu^{3+}) into the AC/IS hybrid matrix. The presence of the IL in ACPTMS could be confirmed by the presence of the absorption band at 1562 cm^{-1} (C=C aromatic) [33] in the spectra of both doped (AC/IS-Ln) and non-doped (AC/IS) samples (Fig. 3b). It is interesting to

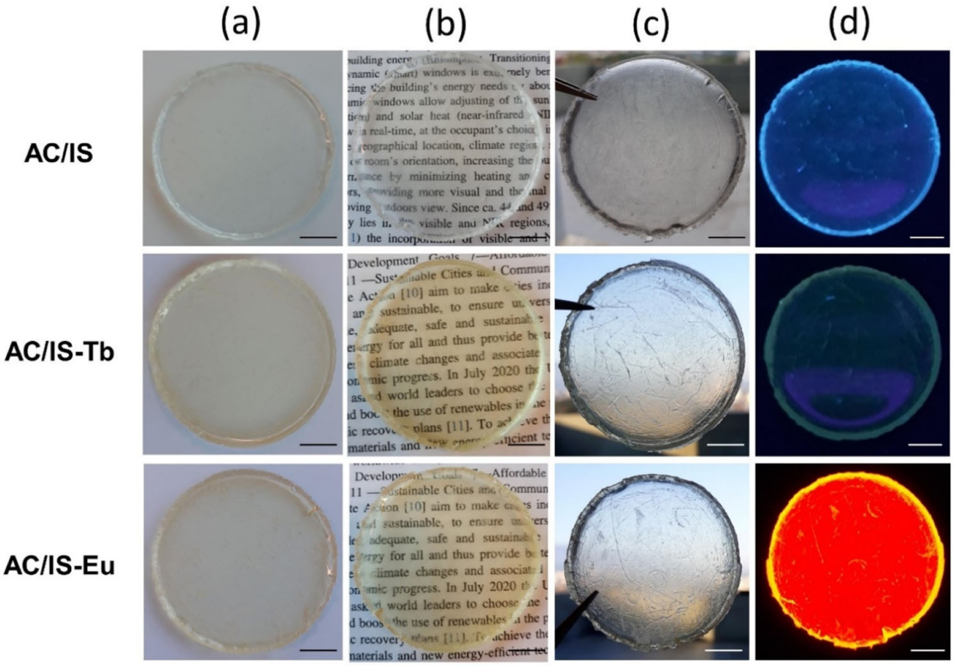

Fig. 2 Physical appearance of the non-doped and doped AC/IS monoliths: under daylight against a white background (**a**), a written background (**b**), and an outside environment (**c**), and under UV light (365 nm) (**d**). The scale bar is 1.0 cm

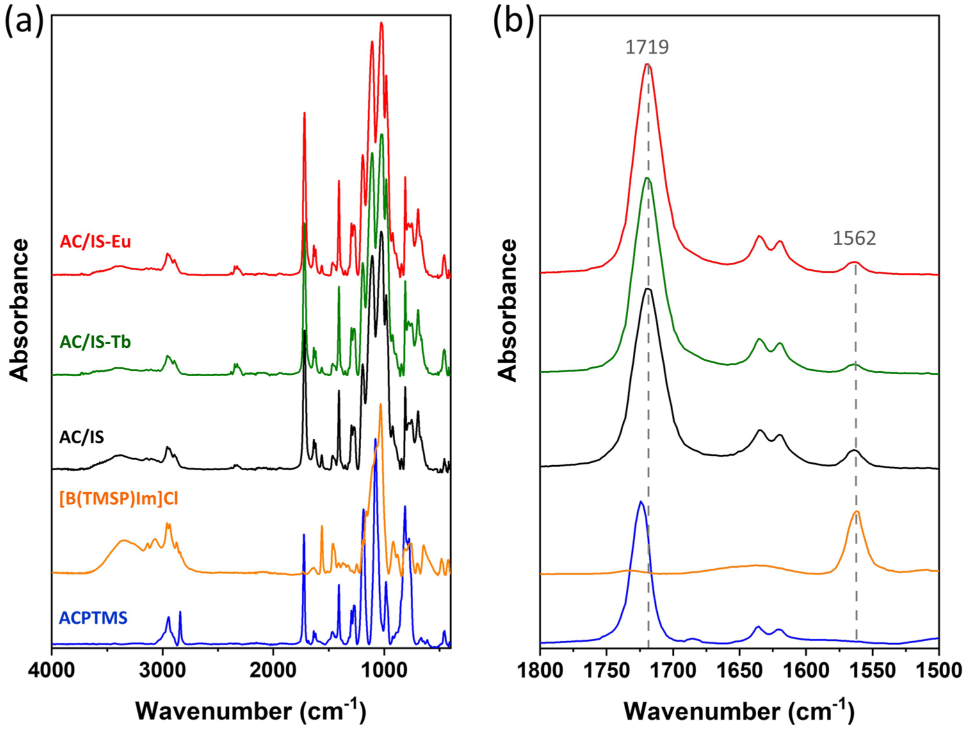

Fig. 3 ATR-FTIR spectra of ACPTMS, [B(TMSP)Im]Cl, AC/IS, AC/IS-Tb, and AC/IS-Eu electrolytes films in the (**a**) 4000–400 cm^{-1} region and (**b**) 1800–1500cm^{-1} region. The lines are just meant to be a guideline for the eye

observe that the strong absorption band at 1724 cm^{-1} from the ACPTMS carbonyl (C=O) group (Fig. 3b, blue line) shifted to lower wavenumbers (ca. 1719 cm^{-1}), upon incorporation of the AC framework into the IS network (AC/IS-Tb, green line; AC/IS-Eu, red line and AC/IS, black line). In the case of the PMMA-based composite films doped with lanthanide-doped sol–gel derived ionosilicas [26, 34], the C=O group band of PMMA remained unshifted, meaning that these groups persisted *quasi* "free", i.e., devoid of any interactions. In the present case, since the shift was observed for the non-doped and doped samples, we are led to the conclusion that the acrylate C=O groups are very likely involved in hydrogen bonding interactions.

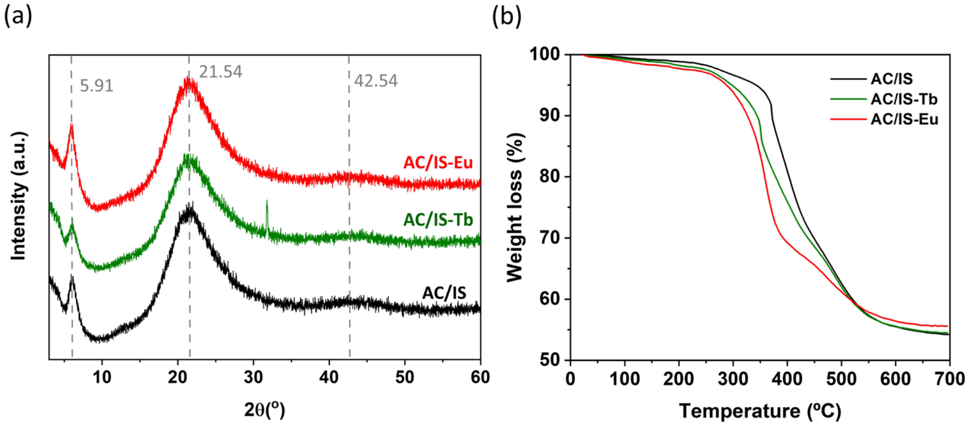

Fig. 4 XRD patterns (**a**) and TGA curves (**b**) of AC/IS, AC/IS-Tb, and AC/IS-Eu

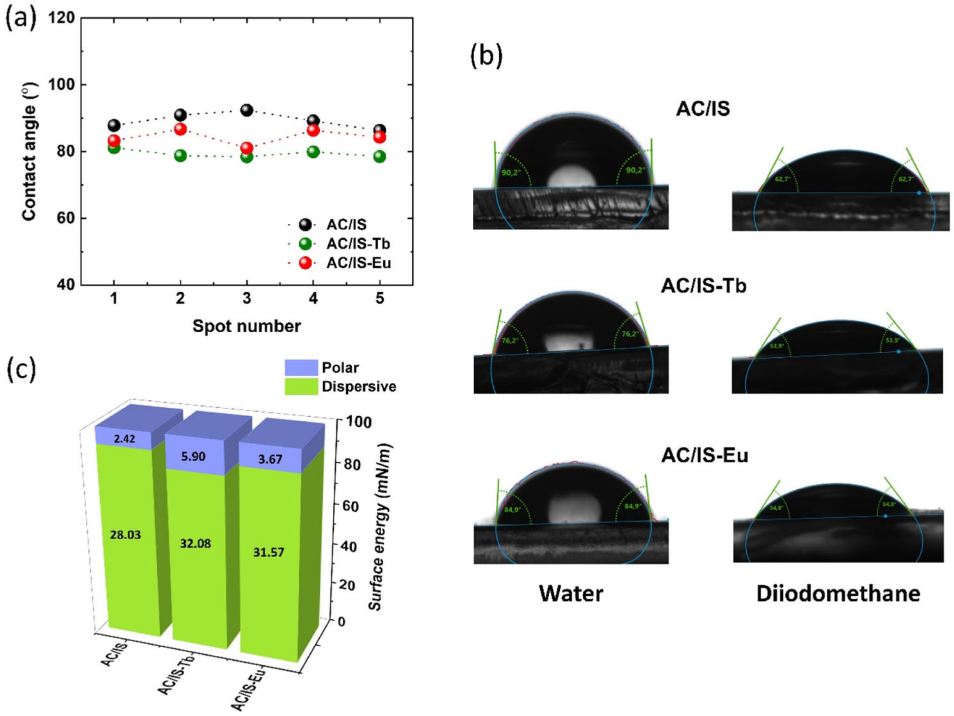

Fig. 5 Static water contact angle of AC/IS, AC/IS-Tb, and AC/IS-Eu (**a**). Photographs of static water and diiodomethane contact angles measurements (**b**). Polar and dispersive values of surface energy (**c**)

The XRD patterns of AC/IS (black line), AC/IS-Tb (green line), and AC/IS-Eu (red line) are shown in Fig. 4a. All the samples exhibit a prominent, broad, Gaussian-shaped peak at ca. 21.54° that was previously ascribed to the coherent diffraction of the siliceous backbone [26, 35, 36]. The structural unit distance, estimated using the Bragg's Law (Eq. (1)), is $d_1 = 0.41$ nm. The 2nd order of this peak appears as a broad weak hump around 42.54°, with a characteristic distance of 0.21 nm [35]. An ill-defined peak is also seen in the pattern of AC/IS (Fig. 4a, black line) at ~12.88° ($d_2 = 0.68$ nm). Additionally, an intense well-defined and sharp peak is detected around 5.91° ($d_3 = 1.50$ nm) in the three samples.

Comparison of these findings with those reported by Belon et al. [37], for organic/inorganic sol–gel materials prepared via a single-step from acrylate trialkoxysilane precursors using a combination of radical and cationic photo processes, is of interest. While the spacings d_1 and d_2 match exactly the present values, the d_3 value found by these authors was 1.39 nm (approximately the double of d_2 ($0.68 \times 2 = 1.36$ nm), which corresponds to the theoretical length of the acrylate chain). This evidence prompted them to propose the formation of a local lamellar organization comprising a double layer structure of organic chains covalently linked by a siloxane backbone. We note that their materials differ from the present ones in the fact that the radical photopolymerization afforded poly(-acrylate) chains, whereas in the AC/IS-based hybrids the acrylate chains were left unreacted, i.e., the allyl groups remained free. In addition, in the case of the AC/IS-based samples, apart from pendant acrylate chains, there is a minor

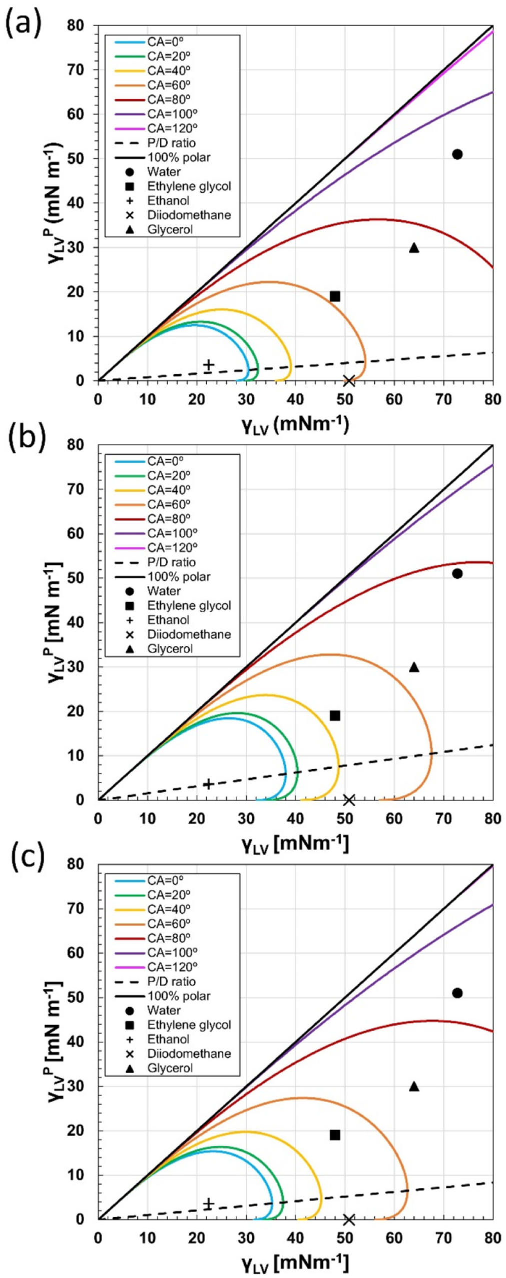

Fig. 6 Wetting envelopes for (**a**) ($\gamma_{\mathrm{LV}} = 30.45\,\mathrm{mN\,m^{-1}}$ and $\gamma^{\mathrm{P}}_{\mathrm{LV}} = 2.42\,\mathrm{mN\,m^{-1}}$), (**b**) ($\gamma_{\mathrm{LV}} = 37.98\,\mathrm{mN\,m^{-1}}$ and $\gamma^{\mathrm{P}}_{\mathrm{LV}} = 5.90\,\mathrm{mN\,m^{-1}}$) and (**c**) ($\gamma_{\mathrm{LV}} = 35.24\,\mathrm{mN\,m^{-1}}$ and $\gamma^{\mathrm{P}}_{\mathrm{LV}} = 3.67\,\mathrm{mN\,m^{-1}}$) electrolyte films. Points representing water, ethylene glycol, ethanol, diiodomethane, and glycerol are plotted

fraction of pendant butylimidazolium-based moieties the length of which is about 1.40 nm, assuming an all-*trans* conformation for the butyl chain [38]. If a lamellar bilayer arrangement of the butylimidazolium-based chains occurred as reported for IS-Eu [26], a low angle peak would be expected corresponding to a spacing of 2.80 nm or slightly less, depending on the degree of chain interpenetration. Considering the low proportion of the latter groups, it is thus not surprising to observe only a reflection at 5.91°.

The thermal behavior of AC/IS, AC/IS-Tb, and AC/IS-Eu samples was studied by TGA (Fig. 4b). The TGA curves evidence a minor weight loss of 3% from 23 to 230 °C, which is ascribed to the release of water molecules [26] and evaporation of solvents [39]. In the 230–700 °C range, the TGA analysis revealed the existence of two main decomposition stages for all the samples with onsets at ~330 and ~460 °C. The first weight loss can be ascribed to the decomposition of the tta$^-$ ligands. The second one can be attributed to the degradation of the Si-O-Si skeleton structure [40, 41]. At the highest temperature examined (700 °C), 44–46% of the AC/IS-based materials remained to be decomposed. The remaining mass is associated with pure silica [42]. AC/IS-Tb and AC/IS-Eu exhibit thermal behavior similar to that of AC/IS, showing that the incorporation of the $[\mathrm{Eu(tta)_4}]^-$ complex anions did not have negative consequences.

To get insight into the wettability and adhesion behavior of the AC/IS, AC/IS-Tb, and AC/IS-Eu electrolyte films, the water/diiodomethane contact angle values were measured, leading to the following results: 91 ± 11/61 ± 3°, 78 ± 5/54 ± 1°, and 84 ± 5/55 ± 2° (Fig. 5), respectively. The water contact angle values reveal the hydrophobic behavior of AC/IS and hydrophilic behavior of AC/IS-Tb and AC/IS-Eu. From these results, it is evident that the static contact angles decreased with the incorporation of the $[\mathrm{Ln(tta)_4}]^-$ complex anions, in particular for $\mathrm{Tb^{3+}}$.

The SFE and the relative proportion of the polar and dispersive components were calculated for all the electrolyte films (Fig. 5c). Values of 0–20 $\mathrm{mJ\,m^{-2}}$ indicate highly hydrophobic character similar to poly(tetrafluoroethylene) (PTFE), whereas values of 20–40 $\mathrm{mJ\,m^{-2}}$ indicate hydrophobic behavior similar to PMMA [43]. The SFEs deduced were 30 ± 5 $\mathrm{mJ\,m^{-2}}$ for AC/IS, 38 ± 3 $\mathrm{mJ\,m^{-2}}$ for AC/IS-Tb, and 35 ± 3 $\mathrm{mJ\,m^{-2}}$ for AC/IS-Eu. Thus, we are led to conclude that all the samples presented a behavior similar to that of PMMA.

Building wetting envelopes is extremely convenient. Several valuable conclusions may be retrieved from Fig. 6. If we consider ethylene glycol ($\gamma_{\mathrm{LV}} = 48\,\mathrm{mN\,m^{-1}}$) and diiodomethane ($\gamma_{\mathrm{LV}} = 50.8\,\mathrm{mN\,m^{-1}}$, cross symbol), we conclude that, although both these solvents have similar γ_{LV} values, for AC/IS diiodomethane and ethylene glycol will produce contact angles of 60° (Fig. 6a), whereas contact angles of nearly 40° and 50° will result for AC/IS-Tb and AC/IS-Eu, respectively (Fig. 6b, c).

AFM analyses were carried out in order to characterize the AC/IS-Ln films in terms of their surface topography. The two-dimensional (2D) and three-dimensional (3D) AFM images are shown in Fig. 7. AFM images revealed that all electrolyte films exhibit smooth surfaces, with average (R_a) surface roughness values of 1.28, 1.22, and 5.20 nm for AC/IS, AC/IS-Tb, and AC/IS-Eu, respectively.

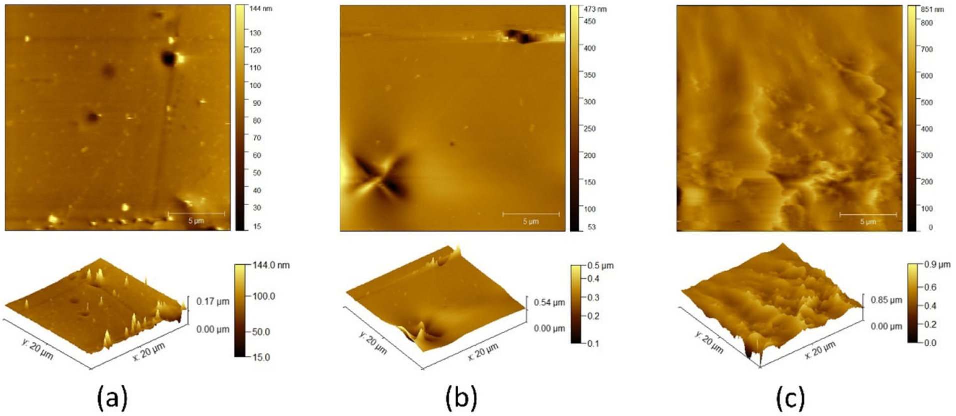

Fig. 7 Topographical AFM images of AC/IS (**a**), AC/IS-Tb (**b**), and AC/IS-Eu (**c**). 2D topography images (top panel) and 3D topography images (bottom panel)

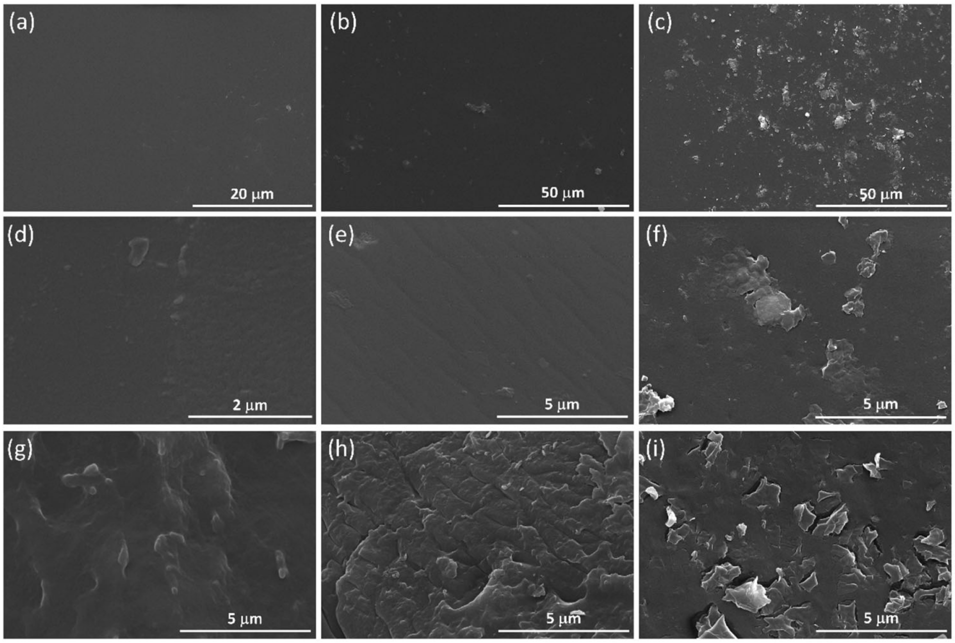

Fig. 8 Surface (**a**–**f**) and cross-section (**g**–**i**) SEM images of AC/IS (**a**, **d**, **g**), AC/IS-Tb (**b**, **e**, **h**), and AC/IS-Eu (**c**, **f**, **i**)

SEM images of the surface of the AC/IS-based films (Fig. 8a–f) reveal that, while AC/IS (Fig. 8a, d) and AC/IS-Tb (Fig. 8b, e) presented a flat surface, AC/IS-Eu (Fig. 8c, f) exhibited some defects, that can be responsible for the small increase of the surface roughness observed by AFM analysis. The cross-section SEM images show that the incorporation of the IS-Ln into the AC led to the increase of porous structures (microaggregates) (Fig. 8h, i). Despite the observed increase of roughness/defects after the addition of IL-Ln to AC, considering that all the samples were obtained as transparent films (Fig. 2b), it can be ascertained that the IS-Ln are well dispersed in the AC framework and that the prepared samples are homogeneous. These results substantiate that the incorporation of IS-Ln did not lead to a dramatical change in the morphology of AC/IS.

3.2 Ionic conductivity

The temperature dependence of the ionic conductivity of AC/IS, AC/IS-Tb, and AC/IS-Eu is depicted in Fig. 9. This plot indicates that the ionic conductivity of AC/IS-Eu at 19 °C (2.39×10^{-6} S cm^{-1}, red line and symbols) is higher than those of AC/IS-Tb at 23 °C (1.07×10^{-6} S cm^{-1}, green line and symbols) and AC/IS at 17 °C (9.54×10^{-8} S cm^{-1}, black line and symbols). In fact, the AC/IS-Eu is more conducting than the sample doped with Tb, and the non-doped sample (AC/IS) over the whole range of temperatures studied. The highest ionic conductivity values of AC/IS-Eu (1.71×10^{-4} S cm^{-1}, red line and symbols), AC/IS-Tb (7.71×10^{-5} S cm^{-1}, green line and symbols), and AC/IS (5.09×10^{-5} S cm^{-1}, black line and symbols) were achieved near 100 °C. From these results, it is clearly seen that the incorporation of the IS-Eu in the AC formulation is advantageous, leading to higher ionic transport.

3.3 Photoluminescence

The room temperature emission spectra of the AC/IS-Tb and AC/IS-Eu samples excited at the wavelength that maximizes the emission intensity are shown in Fig. 10a, which are dominated by the $^5D_4 \rightarrow {}^7F_{6\text{-}0}$ and $^5D_0 \rightarrow {}^7F_{0\text{-}4}$ transitions, respectively. For the case of AC/IS-Eu, no sign of the undoped AC/IS intrinsic emission (Fig. S5 in SI) could be observed, which readily suggests efficient AC/IS-to-ligand/Ln^{3+} energy transfer [44]. For AC/IS-Tb, depending on the excitation wavelength, a band ascribed to the undoped AC/IS may be visible. In naked eye conditions, the emission of AC/IS-Eu is much more noticeable than that of the AC/IS-Tb sample, which is in accordance with the observed absolute emission quantum yield values of 0.24 ± 0.02 and 0.01 ± 0.01, respectively. The lifetime of the emitting states also reveals typical values around 0.326 ± 0.001 ms ($^5D_4$) and 0.505 ± 0.001 ms ($^5D_0$), resulting from the exponential fittings presented in Figs. S6 and Fig. S7 in SI.

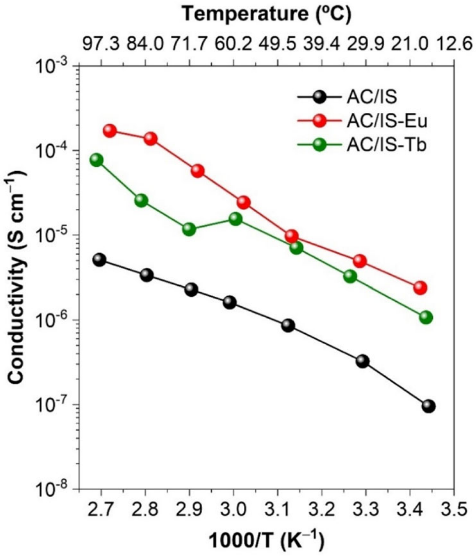

Fig. 9 Ionic conductivity of AC/IS (black line and symbols), AC/IS-Tb (green line and symbols), and AC/IS-Eu (red line and symbols). The lines are meant to be a guide to the eye

The absorption capacity is evidenced in the excitation spectra monitored around the more intense transitions for each case (Fig. 10b). For the AC/IS-Tb, two main components peaking at 280 and 320 nm are ascribed to the π–π* electronic transition of the organic ligands [45], while a broad band is present at around 400 nm, which is also detected in the excitation spectrum of the undoped AC/IS. The excitation spectra revealed the same components around 280 and 320 nm and also a band peaking at 375 nm, ascribed to the organic ligands too [45]. The absorption of the organic groups in the UV region of the solar spectrum is beneficial, allowing possible yellowing phenomena of the AC/IS network to be mitigated.

3.4 Characterization and performance of the prototype ECD

Using a classical five-layer configuration, an ECD including the electrolyte with the highest room temperature ionic conductivity, i.e., AC/IS-Eu (2.39×10^{-6} S cm^{-1}), was assembled (ECD@AC/IS-Eu) (Fig. 1) and its operation tested. As is noticeable in Fig. 11, the ECD containing Eu^{3+} reveals emission under standard solar irradiation (AM1.5) pointing out the potential of the emitting film to be excited under daylight conditions.

As-prepared ECD@AC/IS-Eu exhibited T values of 72 and 56 at 555 and 1200 nm, respectively (Table 1) and a light-yellow (L* = 80.26, a* = −2.11.17 and b* = 11.85) color hue (Fig. 12 and Table S1). The ECD@AC/IS-Eu device was then subjected to three series of cycling steps: (1st series) 6 CV cycling at 50 mV s^{-1} (±1.0 V), followed by CA cycles (0.0 V, 200 s; −1.0 V, 200 s; +1.0 V, 200 s), 6 CV cycling at 50 mV s^{-1} (±1.5 V), followed by CA cycles

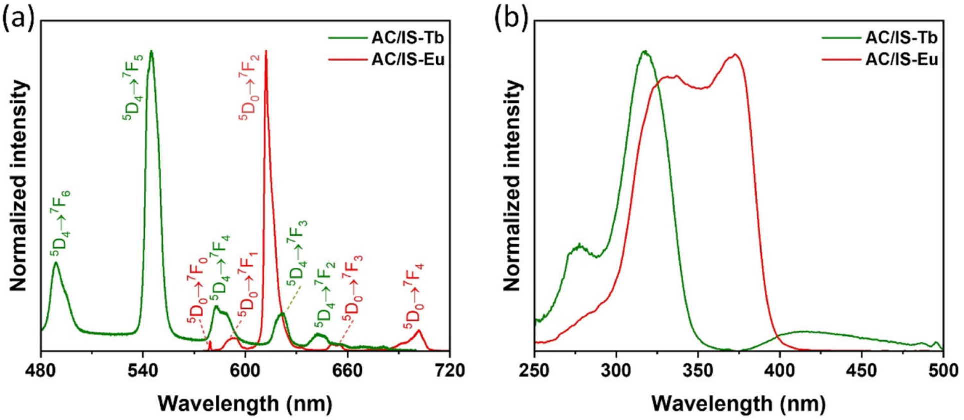

Fig. 10 Room temperature (**a**) emission and (**b**) excitation spectra of AC/IS-Tb (green line) and AC/IS-Eu (red line) excited at 320 and 375 nm and monitored at 544 and 612 nm, respectively

(0.0 V, 200 s; −1.5 V, 200 s; +1.5 V, 200 s), 6 CV cycles at 50 mV s^{-1} (±2.0 V), followed by CA cycles (0.0 V, 200 s; −2.0 V, 200 s; +2.0 V, 200 s) and 6 CV cycles at 50 mV s^{-1} (±2.5 V), followed by CA cycles (0.0 V, 200 s; −2.5 V, 200 s; +2.5 V, 200 s); (2nd series) 10 CA cycles (±2.5 V, 50 s) followed by CA cycles (0.0 V, 200 s; −2.5 V, 200 s; +2.5 V, 200 s); (3rd series) 50 CA cycles (±2.5 V, 50 s).

At the end of CV cycling performed in the 2nd series of measurements (6 CV cycles at ±2.0 and 6 CV cycles at ±2.5 V) (Fig. S8), the ECD@AC/IS-Eu exhibited light blue and dark blue colors, respectively (Fig. 12b, c and Table S1), pushing the T values down to *ca.* 62/47% and 59/38% at 555/1200 nm, respectively (Table S2 and Fig. 12a). Figure 12a, b and Table S2 demonstrate that the T values progressively decreased upon application of the above voltages, and that the corresponding ΔT and ΔOD values increased (at 555/1200 nm: 4.35/5.63%, 6.78/11.16%, and 0.029/0.049, 0.047/0.111 (Table 1), respectively). The results also showed that the ΔT and ΔOD values are always higher in the NIR region than in the visible region. The ECD@AC/IS-Eu prototype device is able to reasonably block visible light and very efficiently block heat, thus lending itself for application in windows in buildings located in hot climate regions.

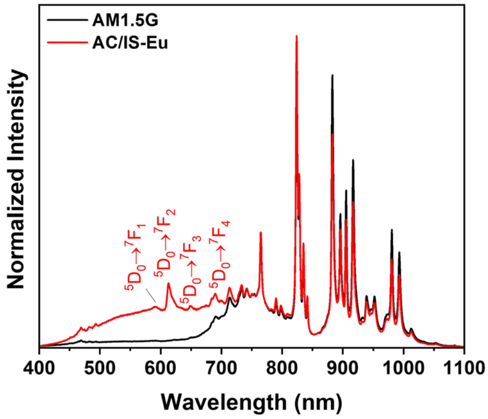

Fig. 11 Room temperature emission spectrum of AC/IS-Eu ECD excited under AM1.5 The solar irradiance spectrum is also shown to render clear the contribution of the intra-4f transitions from the ECD

The chronoamperometry technique was used to evaluate the behavior of the ECD@AC/IS-Eu device over 50 bleaching/coloring CA cycles (±2.5 V at every 50 s). Figure 13a, b and Table S3 allow inferring that the device displayed excellent cycling stability with reproducible bleaching/coloring cycles and excellent optical modulation stability. A high difference between the magnitude of the cathodic and anodic current densities is observed, indicating that the coloring kinetics are considerably faster than the bleaching kinetics. The response times for ECD@AC/IS-Eu were 30–35 s for coloring and 1.0 min for bleaching. This behavior has already been described for ECD prototypes composed of a different transparent conducting oxide (TCO) material (a-IZO) and the same active electrodes (a-WO_3 and c-NiO), and is related to the amorphous and polycrystalline nature of the electrochromic layers, that facilitate the cathodic process over the anodic one [28].

The CE values in six different regions of the CA cycles (Fig. 13a) were measured and the results show that ECD@AC/IS-Eu at 1200 nm yielded higher $-CE_{in}$ and CE_{out} values than at 555 nm (Table 1). The ECD@AC/IS-Eu self-improvement upon cycling for both the visible region (at 555 nm $CE_{in} = -84$ and $CE_{out} = +91$ cm^2 C^{-1} in

Table 1 Electro-optical parameters of the ECD@AC/IS-Eu prototype devices

Hybrid host	Doping agent	TCO[a]	$T_{\text{as-prepared}}$ (%)		Applied voltage (V)	ΔT[c] (%)		ΔOD		CA interval[e]	CE_{in} (cm^2 C^{-1})	CE_{out}	CE_{in}	CE_{out}	Ref.
			555 nm	1200 nm		555 nm	1200 nm	555 nm	1200 nm		555 nm		1200 nm		
ACPTMS	AC/IS-Eu	c-IMO	72	56	±1.5	1.26	4.06	0.008	0.032						This work
					±2.0	4.35	5.63	0.029	0.049						
					±2.5	6.78	11.16	0.047	0.111	I	−76	74	−112	109	
										II	−84	80	−119	114	
										III	−83	92	−118	131	
										IV	−79	73	−110	101	
										V	−80	76	−120	99	
										VI	−84	91	−122	133	
PMMA	PMMA/IS-Nd-19/IS-Eu-1/[BMIm][PF6]-55	a-IZO[b]	79	96[d]	±2.5	16.00	20.00[d]	0.200	0.250[d]		−303	−381	181	228	[28]
IS	IS-Nd-19/IS-Eu-1		75	83[d]	±2.0	3.00	2.00[d]	0.030	0.020[d]		−201	152	−162	123	

[a] Transparent conductive oxide layer

[b] Amorphous indium zinc oxide

[c] 3rd CV cycle

[d] Value obtained at 1000 nm

[e] CA interval analyzed, please see Fig. S9 in SI

Fig. 12 ECD@AC/IS-Eu prototype device. **a** Photographs of the as-prepared and colored (−2.0 V and −2.5 V) states. **b** Transmission spectra in the visible-NIR region: bleached (+1.5 V, +2.0 V and, +2.5 V) and colored (−1.5 V, −2.0 V and, −2.5 V) states. Values measured during CV cycling. **c** 1976 CIE L*a*b* color coordinates. The open circle corresponds to the as-prepared value and the blue and green closed circles correspond to the values after applying voltages of −2.0 V and −2.5 V, respectively

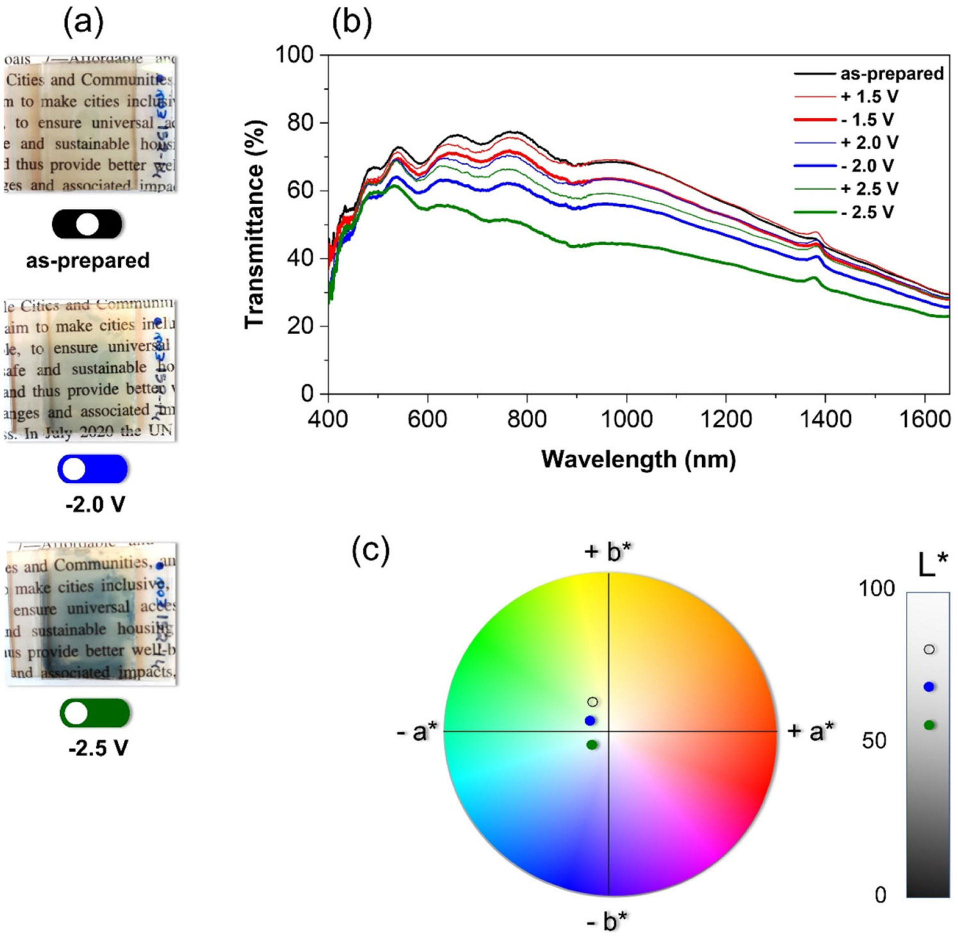

Fig. 13 Electro-optical performance of the ECD@AC/IS-Eu device. **a** Variation of the current density as a function of time over 50 CA cycles at voltage steps of ±2.5 V at every 50 s. The vertical colored bars are the time intervals at which the CE values were calculated. Figure S9 shows a zoom of these intervals. **b** Transmittance at 555 and 1200 nm over 50 CA cycles (bleached state, open symbols and colored state, closed symbols) (Table S2). **c** Optical-circuit memory test

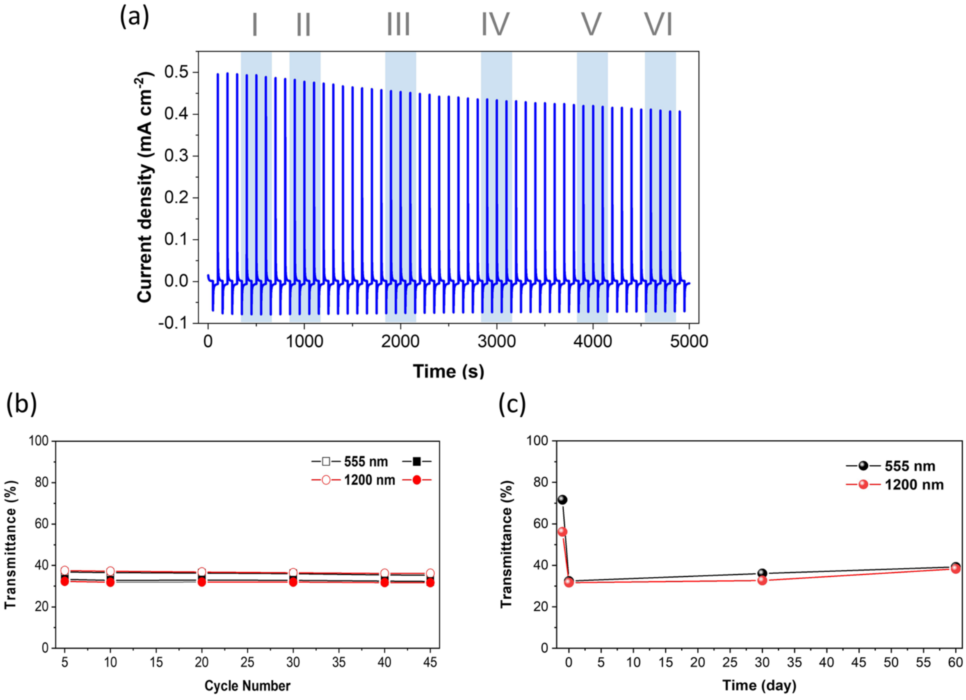

region VI > $CE_{in} = -76$ and $CE_{out} = +74\ cm^2\ C^{-1}$ in region I, Table 1) and the NIR region (at 1200 nm $CE_{in} = -84$ and $CE_{out} = +91\ cm^2\ C^{-1}$ in region VI > $CE_{in} = -122$ and $CE_{out} = +133\ cm^2\ C^{-1}$ in region I, Table 1) is particularly noteworthy. Not surprisingly, this improvement effect is more marked in the case of the bleaching cycles, as a result of the progressive current density decay. The higher CE_{out} values correspond to energetically more efficient bleaching processes requiring less current to induce the same color change.

It is of interest to compare at this stage the best results found in the present work with those reported in the literature for analogous ECDs. The CE values are slightly lower than those of the ECDs incorporating different TCO layers and incorporating PMMA-based systems doped with Ln-doped ionosilicas (PMMA/IS-Nd-19/IS-Eu-1/[BMIm][PF_6]-55) (Table 1). We must note, however, that PMMA/IS-Nd-19/IS-Eu-1/[BMIm][PF6]-55 exhibits much higher room temperature ionic conductivity ($8.76 \times 10^{-4}\ S\ cm^{-1}$ [28]) than AC/IS-Eu ($2.39 \times 10^{-6}\ S\ cm^{-1}$). In the case of an ECD incorporating also a-IZO as TCOs, but incorporating an electrolyte exclusively composed of the mixture of IS-Eu and IS-Nd (IS-Nd-19/IS-Eu-1) (where Nd is neodymium), the ΔT and ΔOD values were higher, but the CE values were slightly lower (Table 1).

Optical memory tests were performed with the ECD@AC/IS-Eu device. Figure 13c demonstrates its exceptionally good performance, since a mere loss of the T value of only 7% occurred after 60 days of being in open circuit in the colored state.

4 Conclusions

In this work, novel lanthanides-containing acrylate/ionosilicas (AC/IS-Ln) were successfully synthesized by sol–gel chemistry, with the goal of developing luminescent hybrids for application in environmentally friendly ECDs enabling the control of the sunlight and solar heat for smart windows of energy-efficient buildings.

The AC/IS-Ln monoliths were produced as homogeneous, transparent and luminescent films, and the structure, topography, surface free energy, ionic conductivity, and optical properties of the electrolyte films were characterized. All the electrolyte films revealed smooth surfaces and hydrophilic behavior.

Photoluminescent studies revealed the typical emission of Eu- and Tb-doped materials upon excitation in the UV spectral range. Because AC/IS-Eu presented the highest ionic conductivity over the whole temperature range examined, it was used as electrolyte in an ECD prototype.

The ECD@AC/IS-Eu prototype demonstrated fast switching time, high switching efficiency, high optical modulation, high coloration efficiency, excellent cycling stability, and outstanding open-circuit memory. This device operation is suitable for windows of buildings located in a hot climate region. Major advantages of the present ECD design are, thus, the reasonable attenuation of glare and the significant reduction of heat consumption due to the voltage-controlled visible/NIR blocking function. In short, this ECD offers a bright hot mode and semi-bright warm mode.

The presence of abundant pendant allyl groups in the materials formulation offers the possibility for further functionalization, in particular crosslinking upon controlled exposure to UV light (ongoing work), as well as the use of UV-patterning procedures, which allows foreseeing applications others than the one proposed here.

Data availability

Data will be made available on request.

Supplementary information The online version contains supplementary material available at https://doi.org/10.1007/s10971-024-06342-8.

Acknowledgements This work was funded by project I&D&I OBTain, operation no. NORTE-01-0145-FEDER-000084, co-financed by the European Regional Development Fund (FEDER) thought NORTE 2020 (Northern Regional Operational Programme 2014/2020), CENTRO2020 in the scope of the project PLANETa, CENTRO-01-0247-FEDER-181242, SOLPOWINS-Solar-Powered Smart Windows for Sustainable Buildings (PTDC/CTM/4304/2020), CQ-VR that is supported by FCT through the projects UIDB/00616/2020 and UIDP/00616/2020 and developed within the scope of the project CICECO-Aveiro Institute of Materials, UIDB/50011/2020, UIDP/50011/2020 & LA/P/0006/2020, Instituto de Telecomunicações (FCT Ref. UIDB/50008/2020) financed by national funds through the FCT/MCTES (PIDDAC), and CQ-University of Minho that is supported by FCT through the projects UIDB/00686/2020 and UIDP/00686/2020. DP acknowledges OBTain for post-doc grant BIPD/UTAD/19/2021. RFPP acknowledges FCT-UMinho for the contract in the scope of Decreto-Lei 57/2016 57/2017. SFHC thanks FCT for a research contract 2022.03740.CEECIND.

Author contributions DP: conceptualization, methodology, validation, formal analysis, investigation, writing—original draft, writing—review and editing, visualization. RFPP: formal analysis, investigation, writing—original draft. AG: resources, investigation. SFHC: formal analysis, investigation. MMS: validation. EF: resources, validation. MCG: validation, supervision. RASF: validation, writing—review and editing. VdZB: conceptualization, validation, writing—review and editing, visualization, supervision, project administration, funding acquisition.

Funding Open access funding provided by FCT|FCCN (b-on).

Compliance with ethical standards

Conflict of interest The authors declare no competing interests.

References

1. Energy performance of buildings directive. Eur Commun https://energy.ec.europa.eu/topics/energy-efficiency/energy-efficient-buildings/energy-performance-buildings-directive_en. Accessed June 2023
2. Energy efficiency directive. Eur Commun. https://energy.ec.europa.eu/topics/energy-efficiency/energy-efficiency-targets-directive-and-rules/energy-efficiency-directive_en. Accessed June 2023
3. 2030 climate targets. Eur Commun. https://climate.ec.europa.eu/eu-action/climate-strategies-targets/2030-climate-energy-framework_en. Accessed June 2023
4. 2050 long-term strategy. Eur Commun. https://climate.ec.europa.eu/eu-action/climate-strategies-targets/2050-long-term-strategy_en. Accessed June 2023
5. Nearly zero-energy buildings. Eur Commun. https://energy.ec.europa.eu/topics/energy-efficiency/energy-efficient-buildings/nearly-zero-energy-buildings_en. Accessed June 2023
6. The Paris Agreement. United Nations. https://www.un.org/en/climatechange/paris-agreement. Accessed June 2023
7. The European Green Deal. Eur Commun. https://commission.europa.eu/strategy-and-policy/priorities-2019-2024/european-green-deal_en. Accessed June 2023
8. Ding Y, Wang M, Mei Z, Diao X (2022) Different ion-based electrolytes for electrochromic devices: a review. Sol Energy Mater Sol Cells 248:112037. https://doi.org/10.1016/j.solmat.2022.112037
9. Primiceri V, Pugliese M, Prontera CT, Monteduro AG, Esposito M, Maggiore A, Cannavale A, Giannuzzi R, Gigli G, Maiorano V (2022) Low-cost gel polymeric electrolytes for electrochromic applications. Sol Energy Mater Sol Cells 240:111657. https://doi.org/10.1016/j.solmat.2022.111657
10. Gu C, Jia A-B, Zhang Y-M, Zhang SX-A (2022) Emerging electrochromic materials and devices for future displays. Chem Rev 122(18):14679–14721. https://doi.org/10.1021/acs.chemrev.1c01055
11. Davy NC, Sezen-Edmonds M, Gao J, Lin X, Liu A, Yao N, Kahn A, Loo Y-L (2017) Pairing of near-ultraviolet solar cells with electrochromic windows for smart management of the solar spectrum. Nat Energy 2(8):17104. https://doi.org/10.1038/nenergy.2017.104
12. Jelle BP, Breivik C (2012) State-of-the-art building integrated photovoltaics. Energy Procedia 20:68–77. https://doi.org/10.1016/j.egypro.2012.03.009
13. Kou Z, Wang J, Tong X, Lei P, Gao Y, Zhang S, Cui X, Wu S, Cai G (2023) Multi-functional electrochromic energy storage smart window powered by CZTSSe solar cell for intelligent managing solar radiation of building. Sol Energy Mater Sol Cells 254:112273. https://doi.org/10.1016/j.solmat.2023.112273
14. Meng Y, Tan Y, Li X, Cai Y, Peng J, Long Y (2022) Building-integrated photovoltaic smart window with energy generation and conservation. Appl Energy 324:119676. https://doi.org/10.1016/j.apenergy.2022.119676
15. O'Regan B, Grätzel M (1991) A low-cost, high-efficiency solar cell based on dye-sensitized colloidal TiO2 films. Nature 353(6346):737–740. https://doi.org/10.1038/353737a0
16. Carella A, Centore R, Borbone F, Toscanesi M, Trifuoggi M, Bella F, Gerbaldi C, Galliano S, Schiavo E, Massaro A, Muñoz-García AB, Pavone M (2018) Tuning optical and electronic properties in novel carbazole photosensitizers for p-type dye-sensitized solar cells. Electrochim Acta 292:805–816. https://doi.org/10.1016/j.electacta.2018.09.204
17. Najm AS, Alwash SA, Sulaiman NH, Chowdhury MS, Techato K (2023) N719 dye as a sensitizer for dye-sensitized solar cells (DSSCs): a review of its functions and certain rudimentary principles. Environ Prog Sustain Energy 42(1):e13955. https://doi.org/10.1002/ep.13955
18. Nowsherwan GA, Iqbal MA, Rehman SU, Zaib A, Sadiq MI, Dogar MA, Azhar M, Maidin SS, Hussain SS, Morsy K, Choi JR (2023) Numerical optimization and performance evaluation of ZnPC:PC70BM based dye-sensitized solar cell. Sci Rep. 13(1):10431. https://doi.org/10.1038/s41598-023-37486-2
19. Gianola G, Speranza R, Bella F, Lamberti A (2023) Homo-tandem-bifacial dye-sensitized solar cell: a new paradigm to boost photoconversion efficiency above limit. Sol Energy 265:112116. https://doi.org/10.1016/j.solener.2023.112116
20. Fagiolari L, Varaia E, Mariotti N, Bonomo M, Barolo C, Bella F (2021) Poly(3,4-ethylenedioxythiophene) in dye-sensitized solar cells: toward solid-state and platinum-free photovoltaics. Adv Sustain Syst 5(11):2100025. https://doi.org/10.1002/adsu.202100025
21. Bati ASR, Zhong YL, Burn PL, Nazeeruddin MK, Shaw PE, Batmunkh M (2023) Next-generation applications for integrated perovskite solar cells. Commun Mater 4(1):2. https://doi.org/10.1038/s43246-022-00325-4
22. Ashif M, Farhana M (2023) Promises and challenges of perovskite solar cells: a comprehensive review. BULLET J Multidisiplin Ilmu 2(5):1147–1157
23. Zhang W, Wu X, Xie L, Zhao O, Zhong J, Zeng X, Zou R (2023) Study on the impact of photovoltaic electrochromic modular smart window on indoor environment. Build Environ 238:110381. https://doi.org/10.1016/j.buildenv.2023.110381
24. Ferreira RAS, Correia SFH, Monguzzi A, Liu X, Meinardi F (2020) Spectral converters for photovoltaics—what's ahead. Mater Today 33:105–121. https://doi.org/10.1016/j.mattod.2019.10.002
25. Frias AR, Cardoso MA, Bastos ARN, Correia SFH, André PS, Carlos LD, de Zea Bermudez V, Ferreira RAS (2019) Transparent luminescent solar concentrators using Ln3+-based ionosilicas towards photovoltaic windows. Energies 12(3):451. https://doi.org/10.3390/en12030451
26. Cardoso MA, Correia SFH, Frias AR, Gonçalves HMR, Pereira RFP, Nunes SC, Armand M, André PS, de Zea Bermudez V, Ferreira RAS (2020) Solar spectral conversion based on plastic films of lanthanide-doped ionosilicas for photovoltaics: down-shifting layers and luminescent solar concentrators. J Rare Earths 38(5):531–538. https://doi.org/10.1016/j.jre.2020.01.007
27. Thakur VK, Ding G, Ma J, Lee PS, Lu X (2012) Hybrid materials and polymer electrolytes for electrochromic device applications. Adv Mater 24(30):4071–4096. https://doi.org/10.1002/adma.201200213
28. Cardoso MA, Correia SFH, Gonçalves HMR, Pereira RFP, Pereira S, Maria TMR, Silva MM, Valente AJM, Fortunato E, Ferreira RAS, de Zea Bermudez V (2022) Solar spectral management with electrochromic devices including PMMA films doped with

biluminescent ionosilicas. J Sol Gel Sci Technol 101(1):58–70. https://doi.org/10.1007/s10971-021-05612-z

29. Elangovan E, Gonçalves G, Martins R, Fortunato E (2009) RF sputtered wide work function indium molybdenum oxide thin films for solar cell applications. Sol Energy 83(5):726–731. https://doi.org/10.1016/j.solener.2008.11.001
30. Kaelble DH, Uy KC (1970) A reinterpretation of organic liquid-polytetrafluoroethylene surface interactions. J Adhes 2(1):50–60. https://doi.org/10.1080/0021846708544579
31. Owens DK, Wendt RC (1969) Estimation of the surface free energy of polymers. J Appl Polym Sci 13(8):1741–1747. https://doi.org/10.1002/app.1969.070130815
32. Surface Tension, Surface Free Energy, and Wettability. Nanoscience. https://www.nanoscience.com/techniques/tensiometry/surface-tension-surface-free-energy-and-wettability/. Accessed March 2023
33. Ullah Bhat S, Ahmad Naikoo R, Tomar R (2016) One pot synthesis of tetra-substituted imidazole derivatives by condensation reaction using zeolite H-ZSM 22 as a heterogeneous solid acid catalyst. Int Res J Pure Appl Chem 11(1):1–10. https://doi.org/10.9734/IRJPAC/2016/21443
34. Wang H, Wang Y, Zhang L, Li H (2013) Transparent and luminescent ionogels based on lanthanide-containing ionic liquids and poly(methyl methacrylate) prepared through an environmentally friendly method. RSC Adv 3(22):8535–8540. https://doi.org/10.1039/C3RA40820E
35. Fu L, Sá Ferreira RA, Silva NJO, Carlos LD, de Zea Bermudez V, Rocha J (2004) Photoluminescence and quantum yields of urea and urethane cross-linked nanohybrids derived from carboxylic acid solvolysis. Chem Mater 16(8):1507–1516. https://doi.org/10.1021/cm035028z
36. Carlos LD, Bermudez VdZ, Ferreira RAS, Marques A, Assunção MC (1999) Sol-gel derived urea cross-linked organically modified silicates. 2. Blue-light emission. Chem Mater 11:581–588. https://doi.org/10.1021/cm980373n
37. Belon C, Chemtob A, Croutxé-Barghorn C, Rigolet S, Le Houérou V, Gauthier C (2010) Combination of radical and cationic photoprocesses for the single-step synthesis of organic-inorganic hybrid films. J Polym Sci A Polym Chem 48(19):4150–4158. https://doi.org/10.1002/pola.24182
38. Takahashi N, Hata H, Kuroda K (2010) Anion exchangeable layered silicates modified with ionic liquids on the interlayer surface. Chem Mater 22(11):3340–3348. https://doi.org/10.1021/cm9037439
39. Gonçalves MC, Pereira RFP, Alves R, Nunes SC, Fernandes M, Gonçalves HMR, Pereira S, Silva MM, Fortunato E, Rego R, de Zea Bermudez V (2020) Electrochromic device composed of a di-urethanesil electrolyte incorporating lithium triflate and 1-butyl-3-methylimidazolium chloride. Front Mater 7. https://doi.org/10.3389/fmats.2020.00139
40. Xu J, Zhang Y, Chen H, Liu W, Tang Y (2014) Efficient visible and near-infrared photoluminescent attapulgite-based lanthanide one-dimensional nanomaterials assembled by ion-pairing interactions. Dalton Trans 43(21):7903–7910. https://doi.org/10.1039/C4DT00188E
41. Sun L, Liu Y, Dang S, Wang Z, Liu J, Fu J, Shi L (2016) Lanthanide complex-functionalized polyhedral oligomeric silsesquioxane with multicolor emission covered from 450 nm to 1700 nm. N J Chem 40(1):209–216. https://doi.org/10.1039/C5NJ02105G
42. Bouchal R, Miletto I, Thach UD, Prelot B, Berlier G, Hesemann P (2016) Ionosilicas as efficient adsorbents for the separation of diclofenac and sulindac from aqueous media. N J Chem 40(9):7620–7626. https://doi.org/10.1039/C6NJ01473A
43. Gao Y, Guo R, Fan R, Liu Z, Kong W, Zhang P, Du F-P(2018) Wettability of pear leaves from three regions characterized at different stages after flowering using the OWRK method Pest Manag Sci 74(8):1804–1809. https://doi.org/10.1002/ps.4878
44. Lima PP, Nobre SS, Freire RO, Júnior SA, Sá Ferreira RA, Pischel U, Malta OL, Carlos LD(2007) Energy transfer mechanisms in organic−inorganic hybrids incorporating europium(III): a quantitative assessment by light emission spectroscopy J Phys Chem C 111(47):17627–17634. https://doi.org/10.1021/jp074204e
45. Molina C, Dahmouche K, Messaddeq Y, Ribeiro SJL, Silva MAP, de Zea Bermudez V, Carlos LD (2003) Enhanced emission from Eu(III) β-diketone complex combined with ether-type oxygen atoms of di-ureasil organic–inorganic hybrids. J Lumin 104(1):93–101. https://doi.org/10.1016/S0022-2313(02)00684-1